

Simulation of multi-shell fullerenes using Machine-Learning Gaussian Approximation Potential

C. Ugwumadu,^{*} K. Nepal, R. Thapa, and Y. G. Lee
*Department of Physics and Astronomy,
 Nanoscale and Quantum Phenomena Institute (NQPI),
 Ohio University, Athens, Ohio 45701, USA*

Y. Al Majali and J. Trembly
*Russ College of Engineering and Technology,
 Ohio University, Athens, Ohio 45701, USA*

D. A. Drabold[†]
*Department of Physics and Astronomy,
 Ohio University, Athens, Ohio 45701, USA*
 (Dated: December 15, 2022)

Multi-shell fullerenes "buckyonions" were simulated, starting from initially random configurations, using a density-functional-theory (DFT)-trained machine-learning carbon potential within the Gaussian Approximation Potential (GAP) Framework [Volker L. Deringer and Gábor Csányi, Phys. Rev. B 95, 094203 (2017)]. Fullerenes formed from seven different system sizes, ranging from 60 ~ 3774 atoms, were considered. The buckyonions are formed by clustering and layering starting from the outermost shell and proceeding inward. Inter-shell cohesion is partly due to interaction between delocalized π electrons protruding into the gallery. The energies of the models were validated *ex post facto* using density functional codes, VASP and SIESTA, revealing an energy difference within the range of 0.02 - 0.08 eV/atom after conjugate gradient energy convergence of the models was achieved with both methods.

1. INTRODUCTION

Research on various allotropes of Carbon (C) like diamond, graphite, nanotubes, and fullerenes has been a long-standing endeavor. In recent years, with research shifting to disordered C structures, new carbon materials are being unveiled. Examples of such materials include tetrahedral amorphous Carbon [1, 2], Biphenylene carbon sheets [3], and amorphous graphite (layers of amorphous graphene sheets with topological defects in the planes) [4]. It is known that topological defects present unique and interesting mechanical, structural, thermal, and electronic properties that often have scientific and technological consequences. For instance, Zhang and co-workers discovered amorphous carbon structures with a high fraction of sp^3 bonding, recovered from compression of solid C_{60} under high pressure and high-temperature [5]. The resulting material showed remarkable mechanical and electronic properties, with potential application in photovoltaic systems, requiring high strength and wear resistance. The growing interest in amorphous carbon structure raises the question: what other amorphous carbon materials exist?

Topologically, there are two kinds of fullerenes, classical and non-classical fullerenes. The classical fullerenes obey the isolated pentagon rule [6] while their non-classical counterparts do not, and in addition to the

hexagon rings, non-classical fullerenes contain 4 - 8 member rings. Classical fullerenes, especially C_{60} , have been applied in fuel cell catalysis [7], production of supercapacitors and lithium-ion batteries [8, 9], electromagnetic inference shielding [10], biomedical sciences [11], and even more recently in nano-neuroscience [12]. Applications using non-classical fullerenes are limited by their unique physical and chemical properties, which is a consequence of the variation in their local atomic conformations resulting from the inclusion of the non-hexagonal rings. It becomes apparent that an atomistic understanding of these amorphous fullerenes could present an opportunity for targeted engineering of their structures for advanced technological applications. Research on the synthesis, as well as theoretical study on non-classical single-shell fullerenes, has been reported in a number of publications [13–16]. On the other hand, limited theoretical research exists for non-classical multi-shell fullerenes ("buckyonions"). Any progress in this area would require a fundamental understanding of the formation and inter-layer cohesion mechanism in non-classical buckyonions through molecular dynamics (MD) simulations that allow sampling from an extensive statistical ensemble of the configuration space that are energetically favorable. Some notable research on MD simulation of non-classical buckyonions (but using "precursors") include the work of Los and co-workers [17], who simulated the mechanism of buckyion formation from the annealing of ultra-disperse nano-diamonds at 3000 K using the classical long-range carbon bond-order potential (LCBOPII) [18]. Also, Lau and co-workers [19] investigated the micro-

^{*} cu884120@ohio.edu

[†] drabold@ohio.edu

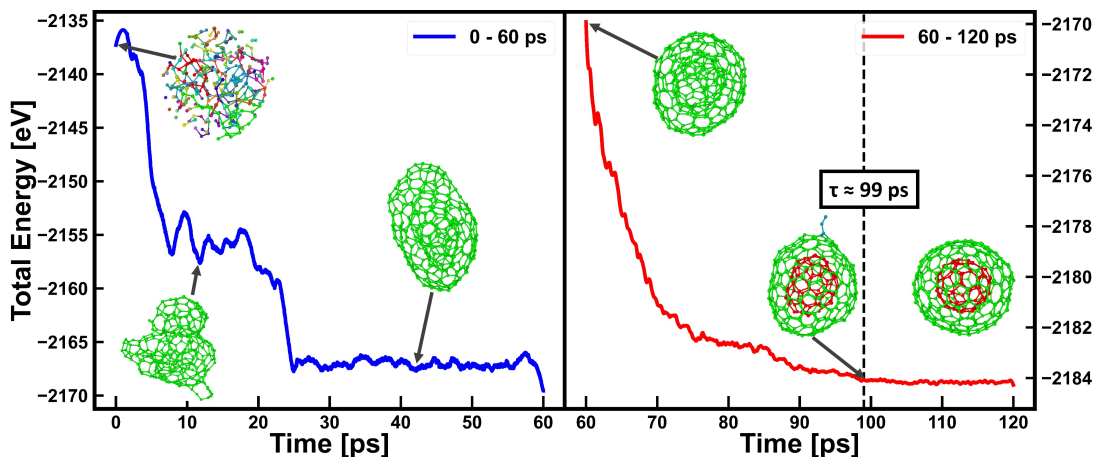


FIG. 1: Shell formation and total energy as a function of simulation time. The insets (shells are colored green and red) show the snapshots of the atomic configurations at different points in time. τ indicates the time at which the shells become visible with significant energy convergence. The right plot (60 - 120 ps) is simply a continuation of the left plot (0 - 60 ps).

structure of buckyonyons formed using pulsed-laser deposition by annealing an a-C structure at 4000 K, using the environment-dependent interaction potential (EDIP) for carbon [20].

This work reports the formation of buckyonyons without any precursor. Starting from a random configuration of carbon atoms with different system size ranging from 60 ~ 3774 atoms, non-classical multi-shell fullerenes (with up to 4 shells) were formed using a density-functional-theory trained machine-learning Gaussian Approximation Potential (GAP) within 40 ~ 130 ps. The buckyonyon models formed were validated through DFT energy minimization in VASP (Vienna Ab initio Simulation Package) [21] and the atomic orbital-based package, SIESTA (Spanish Initiative for Electronic Simulations with Thousands of Atoms) [22]. The multi-shell fullerenes formed up to four shells with topological disorder in each shell (that is, 3D aspherical structures with hexagons, pentagons, heptagons, etc.). Besides a thorough structural investigation with a highly accurate potential, we study mechanisms of formation and the atomistic origins of cohesion in detail. For where it applies, two exchange-correlation functionals were used for the DFT calculations within VASP. These are the generalized gradient approximation (GGA) of Perdew-Burke-Ernzerhof (referred to as PBE) [23] and the combination of the Slater exchange [24] with the Perdew-Zunger parametrization of Ceperley-Alder Monte-Carlo correlation data in the local density approximation [25, 26] (referred to as LDA). However, except where explicitly stated, the results discussed herein are those obtained using the PBE functional.

2. COMPUTATIONAL DETAILS

The models were obtained using the GAP potential for the C-C interaction [27] as implemented within the “Large-scale Atomic/Molecular Massively Parallel Simulator” (LAMMPS) software package [28]. The training of the GAP C potential was based on the conventional method of fitting to an extended set of reference data obtained from simulations based on density functional theory (DFT) [29–32]. Three initial configurations with 60, 300, 540, 840, 1374, 2160, and 3774 atoms were randomly placed to form a spherical bulk with all C atoms being at least 1.45 Å apart. These systems will henceforth be referred to as BO_N , where N is the number of atoms. The bulk was then placed into a cubic box with 3 Å vacuum between the surface of the sphere and the sides of the box so that the periodic boundary condition describes a system of isolated carbon clusters. The atomic positions and velocities were sampled and updated in time-steps of 1 fs from a Nosé-Hoover thermostat at a fixed temperature of 3000 K. The energy trajectories of the systems were analyzed and taken to have reached a satisfactory configuration after negligible energy fluctuations were observed over an extended time period of at least 10 ~ 15 ps. Afterwards, the models were allowed to find a more energetically and structurally favorable configuration by cooling to room temperature at a rate of 2.7×10^{13} K/s, this allowed the systems to attain nearly spherical geometry. Finally, the structures were relaxed using conjugate gradient (CG) algorithm as implemented within LAMMPS with a force tolerance of 10^{-6} eV/Å to obtain a representative structure. Figure 1 presents the time-evolution of the BO_{300} model from one of the initial random configurations to an energetically converged two-layer buckyonyon structure. The parameter τ indicates the time at which the concentric shells become dis-

cernable with essentially non-fluctuating energies. While most of this work was carried out with the aforementioned systems, models with other N were explored for some of the analysis.

The structure and energy of the BO_N models obtained were validated *ex post facto* using VASP and SIESTA. To achieve this, the systems were energetically relaxed using CG algorithm in SIESTA and VASP. Fig. S1 in the supplementary material [33] shows the plots of the energy difference (ΔE) against the CG iterations for $\text{BO}_{300,540,840}$, obtained from the density functional codes. The inset in Fig. S1, representing the GAP model before and after CG relaxation, showed no structural difference in the relaxed models when compared to the original models. The energy difference between the original models and relaxed models (both SIESTA and VASP) ranged within $0.02 \text{ eV/atom} \leq \Delta E \leq 0.08 \text{ eV/atom}$ also with no bond breaking or forming. This is an indication that in the configuration space, the atoms are formed in an energetically stable and realistic local environment. The ‘‘machine learning’’ process involves the absence of an ansatz and a fit of the training (DFT) data to a flexible function. This allows GAP to scan through a wider range of configuration space for a realistic description of structurally complex systems like the buckyonions. In principle, one could model buckyonions from random configurations using *ab-initio* DFT codes like VASP, but this becomes impractical as a result of the plane wave basis set which scales with the cell volume (that contains vacuum). GAP is a real-space method, which is an advantage for molecular systems and also has a computational cost that scales linearly with the system size.

3. STRUCTURAL ANALYSIS

Tables I and II contain information about the simulation parameters and some structural properties calculated for the buckyonion models respectively. Generally, two families of icosahedral multi-shell fullerenes exist, the $60n^2$ and $180n^2$ buckyonions; hence, the smallest shell-unit for buckyonions would be the Buckminsterfullerene (C_{60}) [34]. Variations in the C-C bond-length, as well as Stone-Wales defects in fullerenes, could cause the re-ordering of atoms in the buckyonion layers and yield deviations from the expected shape of the fullerenes. This topological disorder is present in all the buckyonion models and indicated in Fig. 2 (a) and (b) for two independent BO_{60} models. Unlike in C_{60} (see Fig. 2c), which has the expected C-C bond-length ($1.38 \text{ \AA} < x < 1.46 \text{ \AA}$), the BO_{60} and other buckyonions have C-C bond-length ranging from $1.34 \text{ \AA} \sim 1.6 \text{ \AA}$. Furthermore, energy calculation using GAP revealed that the BO_{60} model was 0.03 eV/atom higher in energy compared to pristine C_{60} . Similar calculations for other models are presented in Table III.

The histograms in Fig. 3 (LEFT) represent the ring distribution for some of the BO_N models with the cor-

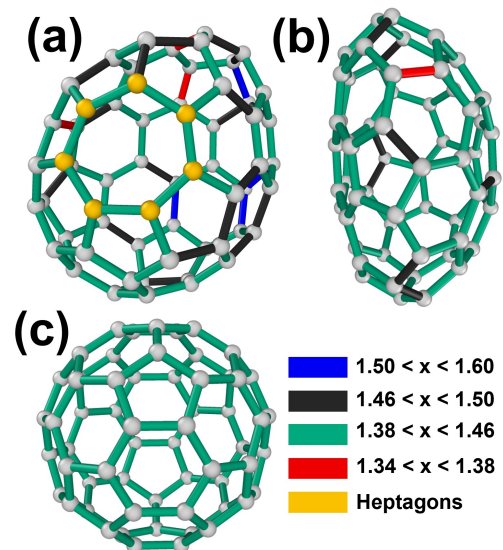


FIG. 2: Topological defects observed in BO_{60} models (a and b). x represents the calculated bond-lengths in \AA . The models are compared with a pristine C_{60} (c) with I_h symmetry [35]

responding bond-angle distribution shown in Fig. 3 (RIGHT). For BO_{1374} , the peaks at 109° and 119° relate directly to the pentagonal and hexagonal atomic arrangements (inset shows a portion of BO_{1374} representative shell with 5- and 6-member rings). On the other hand, the broadening of the angle distribution in BO_{3774} shows variations in ring size. A comprehensive description of the number of ring sizes found in the models is presented in Table S1 [33].

A pentagonal (heptagonal and octagonal) ring in graphitic carbon sheet results in a positive (negative) curvature [37–43]. However, combinations of 5-, 7- and/or 8-member rings in hexagonal carbon networks could result in a complicated morphology [44, 45]. Fig. 4 (a) and (b) show a part of the BO_{840} model with a negative curvature (the 7/8 pairs are colored in blue), while Fig. 4 (c) shows a positive curvature region in BO_{1374} with a high number of pentagons (in red). All the BO_N structures are displayed in Fig. S2 [33]. To form fullerenes, Euler’s polyhedral formula requires a balance in the number of 5/p pairs (p represents 7- or 8- member ring) for an indeterminate number of hexagon rings [39, 46], and any deviation from the 5/p pair at a certain region must be compensated by additional 5-member rings if a positive curvature is to be maintained as shown in Fig. 4 (b).

Even with defects, the number of atoms in the innermost shell for the 300-atom and 520-atom models remained close to 60 and 180 atoms respectively (see Table I), and maintained a nearly spherical geometry in comparison to large N models which are more faceted. This supports experimental evidence that small N buckyonions exist as concentric spherical shells and as faceted structures as N increases [47–52].

TABLE I: Simulation parameters for the buckyunion models.

Model	τ [ps]	Layers	layer Size [number of atoms]			
			s_1	s_2	s_3	s_4
BO ₆₀	41	one	60	-	-	-
BO ₃₀₀	99	two	76	224	-	-
BO ₅₄₀	104	two	174	366	-	-
BO ₈₄₀	119	three	25	282	533	-
BO ₁₃₇₄	109	three	158	456	760	-
BO ₂₁₆₀	113	three	189	799	1172	-
BO ₃₇₇₄	131	four	316	572	1210	1676

TABLE II: Shape descriptors for the buckyunion models.

Model	Gyration radius (R_g) [\AA]			Asphericity (η) [\AA^2]			Anisotropy (κ^2)		
	s_1	s_2	s_3	s_1	s_2	s_3	s_1	s_2	s_3
BO ₆₀	3.57	-	-	0.525	-	-	0.18	-	-
BO ₃₀₀	4.05	6.89	-	0.27	0.43	-	0.03	0.01	-
BO ₅₄₀	6.06	8.9	-	0.71	0.74	-	0.14	0.07	-
BO ₈₄₀	2.4	7.76	10.63	1.48	1.16	1.24	0.12	1.89	0.11
BO ₁₃₇₄	5.84	9.74	12.55	0.85	0.87	0.92	0.19	0.03	0.02
BO ₂₁₆₀	5.88	12.79	15.60	1.69	1.41	1.43	0.18	0.06	0.04
BO ₃₇₇₄	8.19	11.03	16.01	0.46	0.48	0.85	0.01	0.003	0.005
C ₆₀	3.44	-	-	0.01	-	-	≈ 0	-	-
SWCNT	12.78	-	-	144.7	-	-	0.99	-	-
BO ₃₇₇₄	$s_4 = 18.90$			$s_4 = 0.87$			$s_4 = 0.004$		

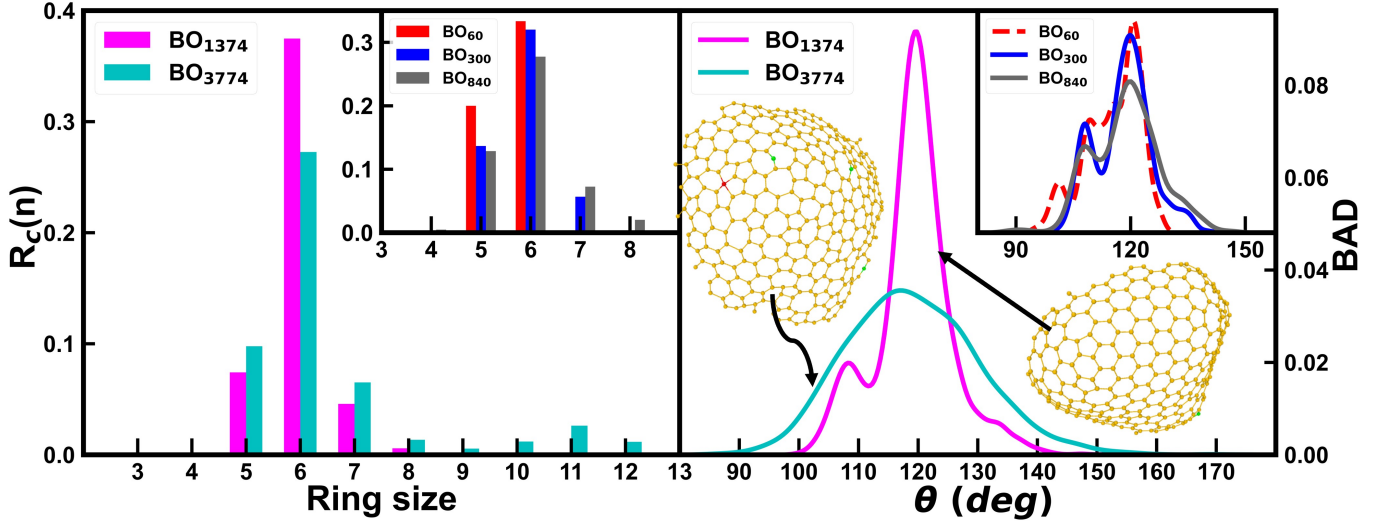


FIG. 3: Ring statistics (LEFT) and bond-angle distribution (RIGHT) for the local environment of the buckyunion models as calculated within ISAACS [36]. The honeycomb structure in the inset is a representative structure for some atoms in BO₁₃₇₄ and BO₃₇₇₄ models.

Further analysis on the shape of the BO_N models was carried out using various shape descriptors derived from the gyration tensor (\mathbf{S}_{ij} ; $i, j = x, y, z$) for each buckyunion shell. The squared radius of gyration (R_g^2) was calculated as the sum of the principal moments (λ_i^2 ; $i = x, y, z$) of the gyration tensor as:

$$R_g^2 = \sum_{i=x,y,z} \lambda_i^2 \quad (1)$$

where the axes were chosen in a way that the principal moments are ordered as $\lambda_z \geq \lambda_y \geq \lambda_x$.

The spherical symmetry of each shell in the buckyunion models was calculated using the asphericity descriptor

TABLE III: Difference in Energy per atom between the buckyion models and C_{60} calculated using GAP ($\delta E_{\text{atom}} = E_{BO_N} - E_{C_{60}}$).

Models	δE_{atom} [eV]	Models	δE_{atom} [eV]
BO ₆₀	0.03	BO ₁₃₇₄	- 0.41
BO ₃₀₀	- 0.30	BO ₂₁₆₀	- 0.43
BO ₅₄₀	- 0.30	BO ₃₇₇₄	- 0.38
BO ₈₄₀	- 0.31		

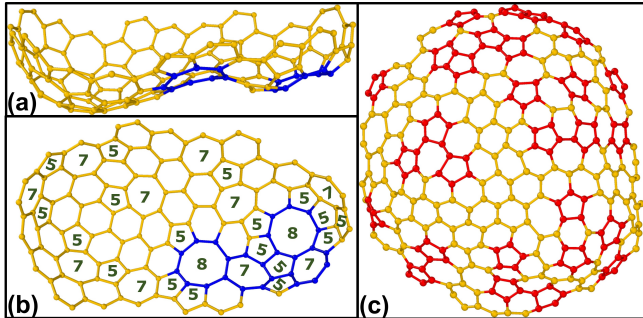


FIG. 4: The surface curvature induced by ring sizes. (a) shows the negative curvature defined by the presence of octagons (blue) and heptagons in (b). (c) shows a positive curvature induced by a large concentration of pentagon (red) in some representative surfaces of the buckyion model.

(η) given as:

$$\eta = \frac{3}{2}\lambda_z^2 - \frac{R_g^2}{2} \quad (2)$$

which is non-negative and is only zero (spherically symmetric) when $\lambda_z = \lambda_y = \lambda_x$. The relative shape anisotropy ($\kappa^2 \in (0, 1)$) was also calculated using the formula:

$$\kappa^2 = \frac{\eta^2 + (3/4)\zeta^2}{R_g^4} \quad (3)$$

where $\zeta = \lambda_y^2 - \lambda_x^2$. κ^2 is 0 for perfectly spherical systems and it is 1 for particles (atoms) that lie on a line. Similar calculations were done for the C_{60} fullerene and a single-walled nanotube to compare with the BO_N model. The results from these calculations are presented in Table II.

Small-angle neutron scattering (SANS) is a valuable technique for structural characterization of fullerenes in solvents with strong SANS contrast (e.g., CS_2) [53–57]. The structures of some BO_N ($N = 60, 70$, and 84) were compared with corresponding structures observed experimentally from the work of Melnichenko and co-workers [58]. Using SANS, they analyzed the shapes of fullerenes

with $N = 60, 70$ and 84 moieties by determining the radius of gyration (R_g) via the standard Guinier approximation of the low- Q end of the scattering profile given as [59]:

$$I(Q) \approx I(0) \cdot \exp\left(\frac{-(QR_g)^2}{3}\right) \quad (4)$$

$I(0)$ is the intensity at zero scattering angle ($Q = 0$). R_g and $I(0)$ are determined from the linear fit to a plot of $\ln(I)$ against Q^2 within the “Guinier region” [60]. Table IV presents values of the radius of gyration from experimental data [55–58], theoretical calculations in ref [58], and those obtained as part of this work for fullerenes with $N = 60, 70$ and 84.

For the 60 atom systems, the result for R_g obtained from this work is consistent with experimental results from the works of Gripon *et al.* [55], Smorenberg *et al.* [56], Spooner *et al.* [57] and those from Melnichenko and co-workers. However, for the 79- and 84- atom systems, experimental data was only available from Melnichenko and co-workers, who also calculated a theoretical radius of gyration from the atomic coordinates of the fullerenes using the Serena Molecular Modeling Software [61]. While there is limited experimental data for structure characterization analysis of buckyions, the ability to reproduce comparable R_g for available fullerenes still serves as a validation for the structure of the BO_N models.

The process of buckyion formation by clustering was investigated by creating two randomly distributed hemispherical clusters with 36 atoms in the first cluster (red atoms in Fig. 5) and 152 atoms in the second cluster (green atoms in Fig. 5). The systems were separated by a distance of at least 3.0 Å and the simulation protocol was the same as described in Sect. 2. Fig. 5 shows that there was hardly any mixing between atoms in both clusters, i.e. the inner shell was formed majorly by atoms in the 36-atom system and the outer shell was formed by atoms in the 152-atom system. This suggests that, even with random configurations, if clustering exists within the system, the buckyion will likely form based on those clusters.

TABLE IV: R_g [Å] for fullerenes with $N = 60, 70$, and 84 obtained from experimental and theoretical (calculated from atomic coordinates in ref [58]) data, compared with corresponding models created using the GAP Potential

	60 atoms	70 atoms	84 atoms
Exp. [55]	3.5 ± 0.20	-	-
Exp. [56]	3.52 ± 0.04	-	-
Exp. [57]	3.57 ± 0.00	-	-
Exp. [58]	3.56 ± 0.05	3.92 ± 0.05	4.27 ± 0.06
Theo. [58]	3.55	3.87	4.19
This work	3.57	3.78	4.05

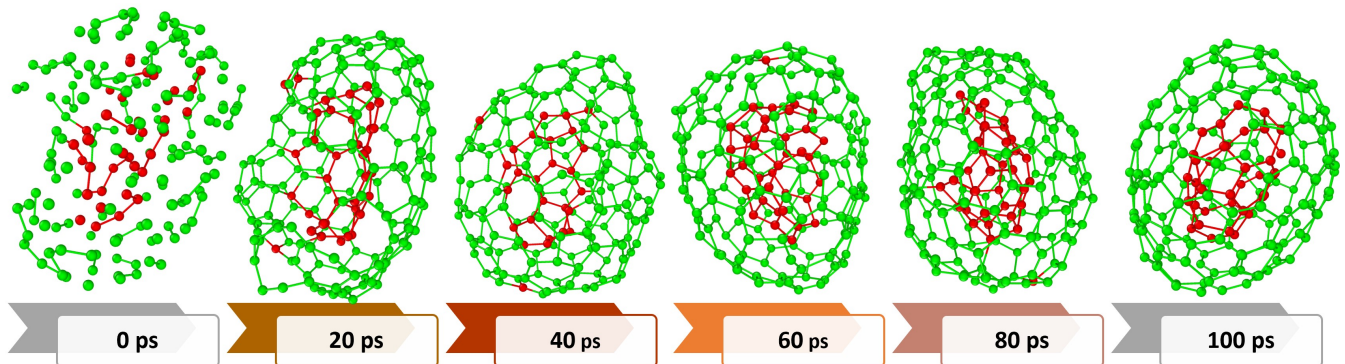


FIG. 5: Clustering Process for buckyunion formation from two bowl-shaped, randomly distributed clusters with 36- (red) and 152- (green) atoms.

Next, the structural order of the BO_N models and pristine C_{60} [35] were analyzed using pair-correlation functions. The first peak in the plot for the radial distribution functions for all the configurations in Figure 6 is centered around the “graphitic” bond-length and the width of the peak indicates disorder-induced deviations from the bond-length. The continuous peaks in the BO_N models overlap with the discrete peaks in C_{60} , which is a validation of the amorphous structure of the buckyunion models.

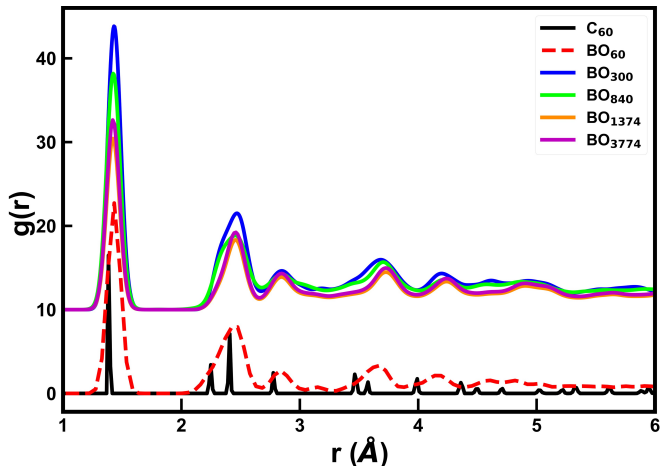


FIG. 6: Radial distribution function $g(r)$ for C_{60} fullerene (in black) and some of the BO_N models. Plots were vertically shifted for clarity.

The gallery width between any two concentric shells was calculated as the difference of the radii between two concentric shells measured from the centroid of the system. The inter-layer separation between the outermost concentric shell showed a consistent value around 2.87 Å for all the models. This value is less than the inter-layer separation observed in pristine Carbon nano-onions (≈ 3.5 Å) [62–64]. In the animation for the formation of BO_{300} and BO_{1374} provided in the supplementary material [33], the path of buckyunion formation brings about

the creation of the outermost layer, and then the system slowly forms inner shells. The animation for BO_{1374} confirms that an initial cluster of atoms exists, which is then shaped spherically, followed by the formation of an outermost layer (green shell) with the inner (still random) cluster separated from the outermost shell. Next, a second layer is formed (red shell), which achieves a stable geometry after a considerable amount of time. After this stage has been completed, the formation of the innermost (blue shell) layer commences. The formation process, combined with the consistent gallery width between the two outermost shells, suggests a level of stability in the outer-shell formation process of the buckyonions. The stability of the outer-shell and the fullerene growth process was further confirmed by creating a randomly distributed 540-atom cluster inside a 720-atom spherical fullerene isomer [35], following the simulation process in Sect. 2. Fig. S3 [33] shows the evolution of the system with observable faceting occurring at regions with pentagons in the outermost shell. Analysis of the number of atoms in each shell revealed that the outermost shell remained with 720 atoms (green shell) throughout the simulation while forming two inner-shells with 364 (red shell) and 176 (blue shell) atoms. This is shown in the animation for the growth process (BO growthProcess.mp4) provided in the supplementary material [33].

4. ELECTRONIC STRUCTURE AND CHARGE DENSITY DISTRIBUTION

The electronic properties of the models were analyzed from calculations of the electronic density of states (EDoS) and the localization of Kohn-Sham states (ϕ) was calculated as the corresponding electronic inverse participation ratio (EIPR), which is given by:

$$I(\phi_n) = \frac{\sum_i |c_n^i|^4}{(\sum_i |c_n^i|^2)^2} \quad (5)$$

where c_n^i is the contribution to the eigenvector (ϕ_n) from

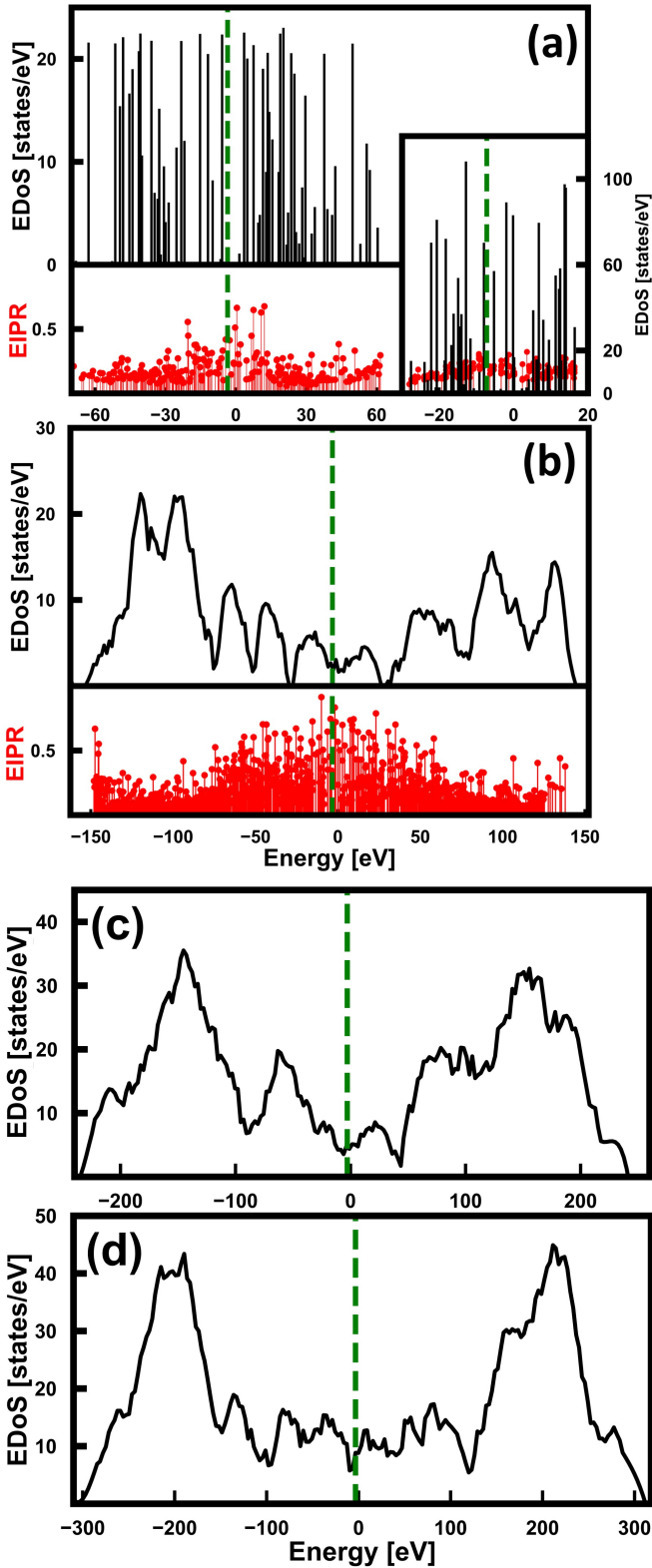


FIG. 7: EDoS and EIPR for (a) BO_{60} , C_{60} [35] (inset) and (b) BO_{300} . EDoS was also computed for (c) BO_{840} and (d) BO_{1374} . The Fermi Energy for all plots is represented as a green vertical-dashed line. The calculations were implemented in SIESTA

the i^{th} atomic orbital (s and p) as implemented within SIESTA using the LDA self-consistent energy functional with a single ζ basis set. Low EIPR values correspond to highly extended states (evenly distributed over N atoms) and high EIPR values describe localized states. Fig. 7 (a) shows the EDoS and EIPR for the BO_{60} model and pristine C_{60} fullerene (inset in 7 (a)). While discrete states were observed for the C_{60} and BO_{60} models, the structural symmetry present in C_{60} fosters degeneracy in its electronic density of states; therefore, electronic states occupying the same energy level (extended EIPR with low values) exists. On the other hand, the absence of certain structural symmetries in BO_{60} resulted in moderately localized states over a wider energy range, breaking the electronic degeneracy. Similar high EIPR values were calculated for BO_{300} (see Fig. 7 (b)), but unlike in BO_{60} , the states in BO_{300} were distributed in a continuous spectrum suggesting non-degeneracy in its energy landscape.

The electronic density of states in the vicinity of the Fermi energy (E_f) is important to many physical properties like transport and superconductivity. The conducting behavior of graphite is a consequence of the absence of any overlap in the valence (π) and conduction (π^*) bands at E_f . Drabold and co-workers, in their work on the spectral properties of large single-shell fullerenes [65], reported the narrowing of the E_f gap as the number of atoms increases. In this work, the EDoS plot shows a gap for BO_{60} at E_f , while for larger BO_N models do not have any gap at E_f (see Fig. 7 (c) and (d) for BO_{840} and BO_{1374} respectively, with states engulfed around E_f). This behavior has been investigated by Liu and co-workers [66], using the scanning tunneling spectroscopy technique, from which they observed that small- N buckyonions were semi-conducting, and increasing metallic properties were observed with increasing N , and hence with an increasing number of shells as well.

Inter-layer cohesion in layered carbon structures like graphite and amorphous graphite derive from a combination of Van der Waals forces, as well as delocalized π electrons in the galleries [4, 67]. This non-dispersive contribution, involving weak “metallic” interactions between the quasi-free electrons, was proposed by Rozploch and co-workers [67, 68]. Interpretation of the contribution of the π electrons to inter-layer cohesion requires a calculation of the individual contribution of the wavefunctions (Kohn-Sham orbitals) describing the system. Therefore, within the interpretation of the DFT formalism, the distribution of the delocalized electron gas in the gallery was investigated using electronic charge density distribution. The total charge density was calculated using both PBE and LDA functionals for BO_{300} models. The obtained values were spatially projected on a $240 \times 240 \times 240$ grid. The average charge density contribution from all the bands is presented in Table V, and five cross-sections of the total charge distribution between two shells (in the $-xz$ plane) are shown in Fig. 8.

In subsequent discussions on Fig. 8, $R_j C^k$ represents

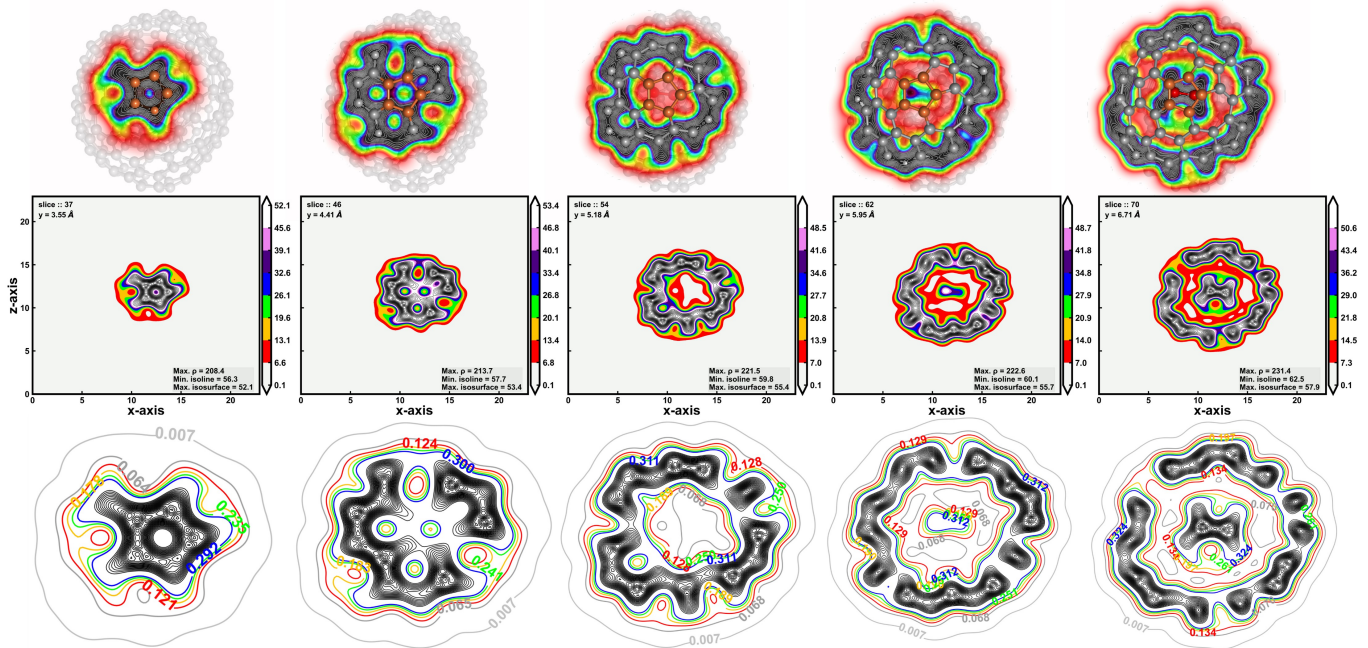


FIG. 8: Cross-sections of the charge density [in $e^-/\text{\AA}^3$] distribution between 2 shells in a BO_{300} model. The charge density values were scaled by a factor of 100. The location of atoms, isosurface, and contour plots for 5 slices are presented in the first (R_1), second (R_2), and third (R_3) row. The columns ($C^1 - C^5$) show the progression from the outer to the inner shell. C^3 is the mid-slice between C^1 and C^5 , and C^2 (C^4) is the mid-slices between C^3 and C^1 (C^5). The charge distribution in the opposite end of the plane considered here is shown in the supplementary material [33].

TABLE V: Average PBE and LDA values for the total and π orbital charge densities for BO_{300} on a 240-bin 3D grid.

Avg. Charge Density	PBE [$e^-/\text{\AA}^3$]	LDA [$e^-/\text{\AA}^3$]
All bands		
Supercell :	2.199 ± 0.035	2.201 ± 0.035
Gallery :	0.095 ± 0.007	0.096 ± 0.005
π bands		
Supercell :	0.543 ± 0.037	0.548 ± 0.037
Gallery :	0.021 ± 0.001	0.020 ± 0.001

the position defined by row j ; column k . Using only R_i (C^i) refers to all the columns (row) in the i^{th} row (columns). R_1 , R_2 , and R_3 show the location of atoms, isosurface, and contour plots for each cross-sectional slice respectively. $C^1 - C^5$ show the progression from the outer to the inner shell. C^3 is the mid-slice between C^1 and C^5 , and C^2 (C^4) is the mid-slice between C^3 and C^1 (C^5). The charge density values in R_2 were scaled by a factor of 100. As a guide, the first set of atoms contributing to the charge density from both shells of the buckyonion, shown in R_1C^1 and R_1C^5 are colored in brown and red. Table V shows that the average charge density in

the mid-gallery region is $\approx 4.3\%$ of the maximum charge density in the supercell. The low charge density values at the mid-gallery region are consistent with results from crystalline graphite (almost zero at the mid-gallery) and amorphous graphite (mid-gallery value was at least 2% of the maximum value of charge density in the system)[4]. The higher values calculated for buckyonions could be a consequence of increased π electron mixing due to the local atomic curvature. For completeness, Fig. S4 shows the charge density plot for the last 5 cross-sectional slices at the opposite end of the model shown in Fig. 8. Additionally, an animation (“TotalChgDensity.mp4”) that shows the progression of the total charge density in the $-xz$ plane along the y -direction is provided in the supplementary material. The animation confirms that the distribution of electrons in the gallery influences inter-shell cohesion in buckyonions and the charges are redistributed based on where atoms are located in each shell.

Next, the actual electronic bands contributing to the inter-shell cohesion were obtained from the spatial band decomposition of the π -orbitals from the total charge density in the same 3D 240-grid. The π electron charge density at the mid-section of the $-xz$ plane for a BO_{300} model is shown in Fig. 9. The charge density values were scaled by a factor of 100. The locations of the contributing atoms are shown in Fig. 9 [TOP]. The values for the π electron charge density in the gallery $\approx 0.023 e^-/\text{\AA}^3$, and increases to $\approx 0.033 e^-/\text{\AA}^3$ for atoms in each shell

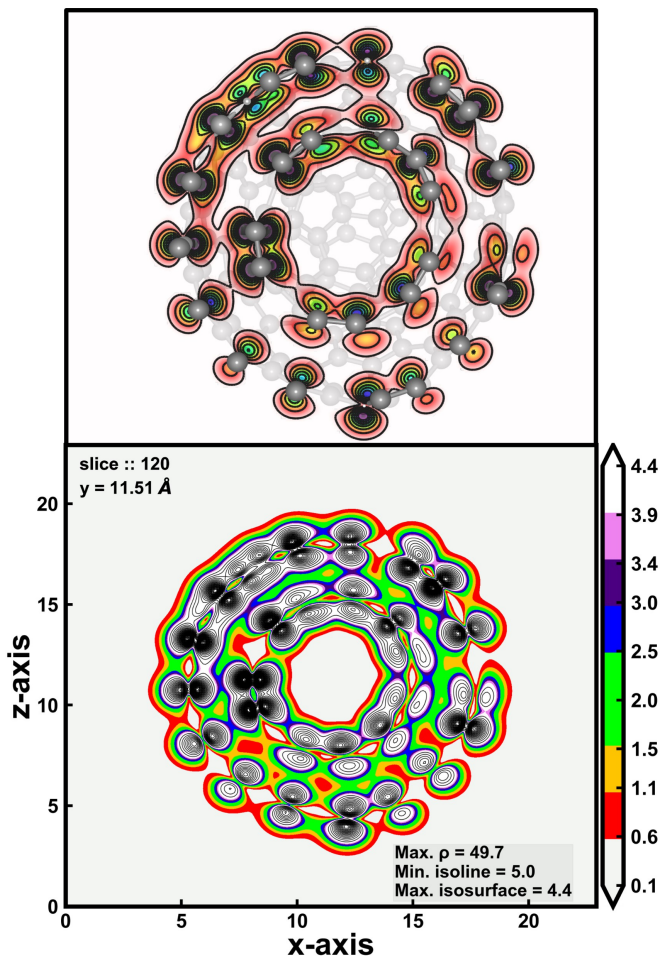


FIG. 9: The delocalized π -electrons in the mid-section of the $-xz$ plane in a BO_{300} model. The PBE functional was used in this calculation and the charge density values were scaled by a factor of 100.

that are positioned opposite each other. In general, the average π electron charge density in the gallery is $\approx 4\%$ of the average in the supercell (see Table V). An animation showing the distribution of the π electrons in a BO_{300} model is also provided in the supplementary material. For comparison, the total and π band charged densities, calculated using LDA functional, showed close values to the results obtained using PBE functional (see Table V). This is also reflected in the close similarity between the isosurface plot in Fig 9 and its LDA-calculated counterpart in Fig S5 [33]. Finally, the contribution of individual π bands to inter-layer cohesion was also investigated. The plots in Fig. 10, which has charge density values scaled by a factor of 1000, show the isosurface of 4 (7) bands below (above) the 600th band which contains the Fermi level (Fermi band), which corresponds to the π (π^*) orbitals. To obtain finer isosurfaces, the grid bin size was increased to $360 \times 360 \times 360$. The average contribution of the π^* electrons in the gallery is (at most) 2 orders of magnitude less than values from the

π bands which means that the delocalized π electrons are the major contributions to the inter-layer cohesion. The results also show that contributions from more than one band can be localized in a particular atom which means that the π bands are linear combinations (mixing) of the wavefunctions (Kohn-Sham orbitals) that describe the buckyonions. It is noteworthy that in these non-classical fullerenes, layering persists despite the absence of an exact (graphitic) stacking registry.

5. CONCLUSION

In this work, the formation of buckyonions from initial random configurations of carbon atoms was achieved using the GAP potential. The structure formed within 100 ps and DFT energy validation revealed an energy difference in the range of 0.02 - 0.08 eV/atom using VASP and SIESTA. Multi-shell fullerenes with 1 \sim 4 layers were created for atoms ranging from 60 \sim 3774 atoms. While there remains a level of topological disorder in each shell (i.e Stone-Waals defects), the number of atoms in the innermost shell remained close to 60 or 180 atoms. The buckyonions prefer to form starting with the outermost shell and then build inwards with a consistency in gallery width of ≈ 2.87 Å between the two outermost layers. Clustering was proposed as a formation mechanism for the buckyonions. The electronic density of states calculation showed that more states appear in the Fermi Level as N increases. Finally, the physics of inter-shell layering was investigated by considering the charge density in the π subspace. Results showed that delocalization of the π electron led to an electronic charge cloud in the gallery, which causes cohesion between shells.

ACKNOWLEDGMENTS

The authors thank Anna-Theresa Kirchttag for proof-reading the manuscript, the U.S. Department of Energy for support under Grant No. DE-FE0031981, and XSEDE (supported by National Science Foundation Grant No. ACI-1548562) for computational support under allocation no. DMR-190008P

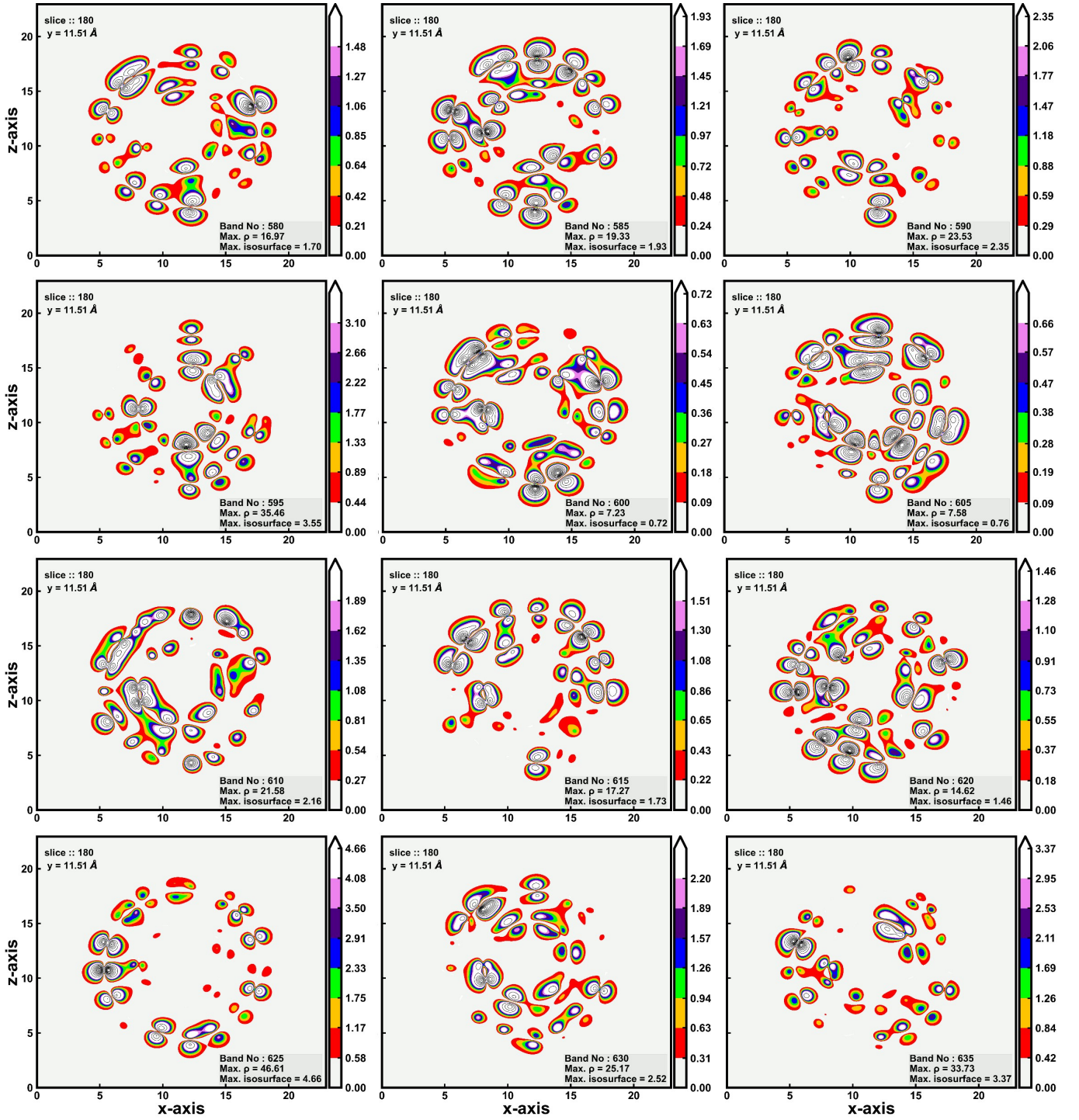


FIG. 10: Single band decomposition of the π electron bands close to the Fermi-level (in the 600th band). 4 (7) bands below (above) the Fermi band are plotted. The charge density values were scaled by a factor of 1000.

[1] D. R. McKenzie, D. Muller, and B. A. Pailthorpe. Compressive-stress-induced formation of thin-film tetrahedral amorphous carbon. *Phys. Rev. Lett.*, 67:773–776, 1991.

[2] D. A. Drabold, P. A. Fedders, and Petra Stumm. Theory of diamondlike amorphous carbon. *Phys. Rev. B*, 49:16415–16422, 1994.

- [3] Qitang Fan, Linghao Yan, Matthias W. Tripp, Ondřej Krejčí, Stavrina Dimosthenous, Stefan R. Kachel, Mengyi Chen, Adam S. Foster, Ulrich Koert, Peter Liljeroth, and J. Michael Gottfried. Biphenylene network: A nonbenzenoid carbon allotrope. *Science*, 372(6544):852–856, 2021.
- [4] R. Thapa, C. Ugwumadu, K. Nepal, J. Trembly, and D. A. Drabold. Ab initio simulation of amorphous graphite. *Phys. Rev. Lett.*, 128:236402, 2022.
- [5] Shuangshuang Zhang, Zihe Li, Kun Luo, Julong He, Yufei Gao, Alexander V Soldatov, Vicente Benavides, Kaiyuan Shi, Anmin Nie, Bin Zhang, Wentao Hu, Mengdong Ma, Yong Liu, Bin Wen, Guoying Gao, Bing Liu, Yang Zhang, Yu Shu, Dongli Yu, Xiang-Feng Zhou, Zhisheng Zhao, Bo Xu, Lei Su, Guoqiang Yang, Olga P Chernogorova, and Yongjun Tian. Discovery of carbon-based strongest and hardest amorphous material. *National Science Review*, 9(1), 2021.
- [6] HW Kroto. The stability of the fullerenes C_n , with $n=24, 28, 32, 36, 50, 60$ and 70 . *Nature*, 329(6139):529–531, 1987.
- [7] Julieta Coro, Margarita Suarez, Lays SR Silva, Katlin IB Eguluz, and Giancarlo R Salazar-Banda. Fullerene applications in fuel cells: A review. *International Journal of Hydrogen Energy*, 41(40):17944–17959, 2016.
- [8] Haibin Wang, Xiaomei Yan, and Guangzhe Piao. A high-performance supercapacitor based on fullerene C_{60} whisker and polyaniline emeraldine base composite. *Electrochimica Acta*, 231:264–271, 2017.
- [9] Zhipeng Jiang, Yuming Zhao, Xing Lu, and Jia Xie. Fullerenes for rechargeable battery applications: Recent developments and future perspectives. *Journal of Energy Chemistry*, 55:70–79, 2021.
- [10] SA Maksimenko, VN Rodionova, G Ya Slepian, VA Karpovich, O Shenderova, J Walsh, VL Kuznetsov, IN Mazov, SI Moseenkov, AV Okotrub, et al. Attenuation of electromagnetic waves in onion-like carbon composites. *Diamond and related materials*, 16(4-7):1231–1235, 2007.
- [11] Jyoti Ahlawat, Shima Masoudi Asil, Gileydis Guillama Barroso, Md Nurunnabi, and Mahesh Narayan. Application of carbon nano onions in the biomedical field: Recent advances and challenges. *Biomaterials Science*, 9(3):626–644, 2021.
- [12] Esmaeel Ghavanloo, Hashem Rafii-Tabar, Ayesha Kausar, Georgios I. Giannopoulos, and S. Ahmad Fazlzadeh. Experimental and computational physics of fullerenes and their nanocomposites: Synthesis, thermo-mechanical characteristics and nanomedicine applications. *Physics Reports*, 996:1–116, 2023.
- [13] Wenyuan Qian, Michael D Bartberger, Salvador J Pastor, Kendall N Houk, Charles L Wilkins, and Yves Rubin. C_{62} , a non-classical fullerene incorporating a four-membered ring. *Journal of the American Chemical Society*, 122(34):8333–8334, 2000.
- [14] Li-Hua Gan, Jian-Qiang Zhao, and Fusheng Pan. Theoretical study on non-classical fullerene C_{54} with square (s) or heptagon (h). *Journal of Molecular Structure: THEOCHEM*, 953(1-3):24–27, 2010.
- [15] Leonid A Openov, Alexei I Podlivaev, and Mikhail M Maslov. Comparative kinetic stability of classical and non-classical fullerenes C_{46} . *Physics Letters A*, 376(45):3146–3149, 2012.
- [16] Jie An, Li-Hua Gan, Xiaoqing Fan, and Fusheng Pan. Fullerene C_{46} : An unexpected non-classical cage. *Chemical Physics Letters*, 511(4-6):351–355, 2011.
- [17] Jan Los, Nicolas Pineau, Guillaume Chevrot, Gerard Vignoles, and Jean-Marc Leyssale. Formation of multiwall fullerenes from nanodiamonds studied by atomistic simulations. *Physical Review B*, 80:155420, 2009.
- [18] Jan H. Los, Luca M. Ghiringhelli, Evert Jan Meijer, and A. Fasolino. Improved long-range reactive bond-order potential for carbon. i. construction. *Phys. Rev. B*, 72:214102, 2005.
- [19] D. W. M. Lau, D. G. McCulloch, N. A. Marks, N. R. Madsen, and A. V. Rode. High-temperature formation of concentric fullerene-like structures within foam-like carbon: Experiment and molecular dynamics simulation. *Phys. Rev. B*, 75:233408, 2007.
- [20] N. A. Marks. Generalizing the environment-dependent interaction potential for carbon. *Phys. Rev. B*, 63:035401, 2000.
- [21] G. Kresse and J. Furthmüller. Efficient iterative schemes for ab initio total-energy calculations using a plane-wave basis set. *Phys. Rev. B*, 54:11169–11186, 1996.
- [22] José M Soler, Emilio Artacho, Julian D Gale, Alberto García, Javier Junquera, Pablo Ordejón, and Daniel Sánchez-Portal. The SIESTA method for *ab initio* materials simulation. *Journal of Physics: Condensed Matter*, 14(11):2745–2779, 2002.
- [23] John P. Perdew, Kieron Burke, and Matthias Ernzerhof. Generalized gradient approximation made simple. *Phys. Rev. Lett.*, 77:3865–3868, 1996.
- [24] Paul AM Dirac. Note on exchange phenomena in the thomas atom. In *Mathematical proceedings of the Cambridge philosophical society*, volume 26, pages 376–385. Cambridge University Press, 1930.
- [25] David M Ceperley and Berni J Alder. Ground state of the electron gas by a stochastic method. *Physical review letters*, 45(7):566, 1980.
- [26] J. P. Perdew and Alex Zunger. Self-interaction correction to density-functional approximations for many-electron systems. *Phys. Rev. B*, 23:5048–5079, May 1981.
- [27] Volker L. Deringer and Gábor Csányi. Machine learning based interatomic potential for amorphous carbon. *Phys. Rev. B*, 95:094203, 2017.
- [28] Aidan P. Thompson, H. Metin Aktulga, Richard Berger, Dan S. Bolintineanu, W. Michael Brown, Paul S. Crozier, Pieter J. in 't Veld, Axel Kohlmeyer, Stan G. Moore, Trung Dac Nguyen, Ray Shan, Mark J. Stevens, Julien Tranchida, Christian Trott, and Steven J. Plimpton. LAMMPS - a flexible simulation tool for particle-based materials modeling at the atomic, meso, and continuum scales. *Computer Physics Communications*, 271:108171, 2022.
- [29] Volker L. Deringer, Albert P. Bartók, Noam Bernstein, David M. Wilkins, Michele Ceriotti, and Gábor Csányi. Gaussian process regression for materials and molecules. *Chemical Reviews*, 121(16):10073–10141, 2021.
- [30] Miguel A. Caro, Gábor Csányi, Tomi Laurila, and Volker L. Deringer. Machine learning driven simulated deposition of carbon films: From low-density to diamond-like amorphous carbon. *Phys. Rev. B*, 102:174201, 2020.
- [31] Volker L. Deringer, Miguel A. Caro, Richard Jana, Anja Aarva, Stephen R. Elliott, Tomi Laurila, Gábor Csányi, and Lars Pastewka. Computational surface chemistry of tetrahedral amorphous carbon by combining machine learning and density functional theory. *Chemistry of Materials*, 30(21):7438–7445, 2018.

- [32] So Fujikake, Volker L. Deringer, Tae Hoon Lee, Marcin Krynski, Stephen R. Elliott, and Gábor Csányi. Gaussian approximation potential modeling of lithium intercalation in carbon nanostructures. *The Journal of Chemical Physics*, 148(24):241714, 2018.
- [33] supplementary materials describing additional properties of the BO_N models.
- [34] S. Iglesias-Groth, A. Ruiz, J. Bretón, and J. M. Gomez Llorente. A theoretical model of the static polarizability of carbon buckyonions. *The Journal of Chemical Physics*, 118(15):7103–7111, 2003.
- [35] David Tománek. *Guide Through the Nanocarbon Jungle*. 2053-2571. Morgan & Claypool Publishers, 2014.
- [36] S Le Roux and V Petkov. Isaacs—interactive structure analysis of amorphous and crystalline systems. *Journal of Applied Crystallography*, 43(11):181, 2010.
- [37] A. L. Mackay and H. Terrones. Diamond from graphite. *Nature*, 352:762, 1991.
- [38] H. Terrones and A.L. Mackay. Hypothetical curved graphite. *Nanostructured Materials*, 3(1):319–329, 1993. Proceedings of the First International Conference on Nanostructured Materials.
- [39] Thomas Lenosky, Xavier Gonze, Michael Teter, and Vert Elser. Energetics of negatively curved graphitic carbon. *Nature*, 355:333–335, 1992.
- [40] David Vanderbilt and J. Tersoff. Negative-curvature fullerene analog of c_{60} . *Phys. Rev. Lett.*, 68:511–513, 1992.
- [41] Rob Phillips, David A. Drabold, Thomas Lenosky, Gary B. Adams, and Otto F. Sankey. Electronic structure of schwarzite. *Phys. Rev. B*, 46:1941–1943, 1992.
- [42] M. Homyonfer, Y. Feldman, L. Margulis, and R. Tenne. Negative curvature in inorganic fullerene-like structure. *Fullerene Science and Technology*, 6(1):59–66, 1998.
- [43] Makoto Tagami, Yunye Liang, Hisashi Naito, Yoshiyuki Kawazoe, and Motoko Kotani. Negatively curved cubic carbon crystals with octahedral symmetry. *Carbon*, 76:266–274, 2014.
- [44] Sumio Iijima. Direct observation of the tetrahedral bonding in graphitized carbon black by high resolution electron microscopy. *Journal of Crystal Growth*, 50(3):675–683, 1980.
- [45] Z. L. Wang and Z. C. Kang. Pairing of pentagonal and heptagonal carbon rings in the growth of nanosize carbon spheres synthesized by a mixed-valent oxide-catalytic carbonization process. *The Journal of Physical Chemistry*, 100(45):17725–17731, 1996.
- [46] Hisashi Naito. Construction of negatively curved cubic carbon crystals via standard realizations. In Yasumasa Nishiura and Motoko Kotani, editors, *Mathematical Challenges in a New Phase of Materials Science*, pages 83–100, Tokyo, 2016. Springer Japan.
- [47] Shoaib Ahmad. Continuum elastic model of fullerenes and the sphericity of the carbon onion shells. *The Journal of Chemical Physics*, 116(8):3396–3400, 2002.
- [48] Enrique Pasqualini. Concentric carbon structures. *Phys. Rev. B*, 56:7751–7754, 1997.
- [49] D. Tomanek, W. Zhong, and E. Krastev. Stability of multi-shell fullerenes. *Phys. Rev. B*, 48:15461–15464, 1993.
- [50] Darrin York, Jian Ping Lu, and Weitao Yang. Density-functional calculations of the structure and stability of C_{240} . *Phys. Rev. B*, 49:8526–8528, 1994.
- [51] Jian Ping Lu and Weitao Yang. Shape of large single- and multiple-shell fullerenes. *Phys. Rev. B*, 49:11421–11424, 1994.
- [52] Mitsuho Yoshida and Eiji Ōsawa. Molecular Mechanics Calculations of Giant- and Hyperfullerenes with Icosahedral Symmetry. *Fullerene Science and Technology*, 1(1):55–74, 1993.
- [53] M. V. Avdeev, T. V. Tropin, I. A. Bodnarchuk, S. P. Yaradaikin, L. Rosta, V. L. Aksenov, and L. A. Bulavin. On structural features of fullerene c_{60} dissolved in carbon disulfide: Complementary study by small-angle neutron scattering and molecular dynamic simulations. *The Journal of Chemical Physics*, 132(16):164515, 2010.
- [54] S. J. Henderson, R. L. Hettich, R. N. Compton, and G. Bakale. Small-angle x-ray scattering and mass spectrometry studies of γ -irradiated c_{60} in cyclohexane. *The Journal of Physical Chemistry*, 100(13):5426–5432, 1996.
- [55] C. Gripon, L. Legrand, I. Rosenman, and F. Boue. Study of Undersaturated C_{60} Solutions in CS_2 by Small Angle Neutron Scattering. *Fullerene Science and Technology*, 4(6):1195–1211, 1996.
- [56] H. E. Smorenburg, R. M. Crevecoeur, I. M. de Scheppe, and L. A. de Graaf. Structure and dynamics of c_{60} molecules in liquid cs_2 from neutron scattering. *Phys. Rev. E*, 52:2742–2752, 1995.
- [57] S Spooner, J. L Zaretsky, and K. A Affholter. Characterization of c_{60} fullerene in carbon disulfide solvent using intermediate angle neutron scattering. In P. Bernier, D. Bethune, L. Y Chiang, T. Ebbeson, R. M. Metzger, and J. W. Mintmire, editors, *Science and Technology of Fullerene Materials*, volume 359, pages 543 – 547, Pittsburgh, Pennsylvania, 1994. Material Research Society.
- [58] Y. B. Melnichenko, G. D. Wignall, R. N. Compton, and G. Bakale. Characterization of fullerenes and fullerene derivatives by small-angle neutron scattering and transmission measurements. *The Journal of Chemical Physics*, 111(10):4724–4728, 1999.
- [59] A. Guinier. *”Small-Angle Scattering of x-rays”*. ”Wiley”, ”New-York”, 1955.
- [60] Christopher D. Putnam. Guinier peak analysis for visual and automated inspection of small-angle X-ray scattering data. *Journal of Applied Crystallography*, 49(5):1412–1419, 2016.
- [61] Alexandru M. Micu and Jeremy C. Smith. Serena: a program for calculating x-ray diffuse scattering intensities from molecular dynamics trajectories. *Computer Physics Communications*, 91(1):331–338, 1995.
- [62] S. Iglesias-Groth, J. Breton, and C. Girardet. An analytical approach for the interlayer interaction in spherical buckyonions. *Chemical Physics Letters*, 264(3):351–358, 1997.
- [63] M. Eugenia Pérez-Ojeda, Edison Castro, Claudia Kröckel, Matteo Andrea Lucherelli, Ursula Ludacka, Jani Kotakoski, Katharina Werbach, Herwig Peterlik, Manuel Melle-Franco, Julio C. Chacón-Torres, Frank Hauke, Luis Echegoyen, Andreas Hirsch, and Gonzalo Abellán. Carbon nano-onions: Potassium intercalation and reductive covalent functionalization. *Journal of the American Chemical Society*, 143(45):18997–19007, 2021.
- [64] Mingguang Yao, Weiwei Zhang, Jiajun Dong, Ran Liu, and Bingbing Liu. Pressure-induced transformations in carbon nano-onions. *Journal of Applied Physics*, 119(23):235902, 2016.
- [65] David A. Drabold, Pablo Ordejón, JianJun Dong, and Richard M. Martin. Spectral properties of large fullerenes: From cluster to crystal. *Solid State Commu-*

- nications*, 96(11):833–838, 1995.
- [66] H.-W Liu, S.-M Hou, S.-J Liu, C.-G Tao, Zujin Shi, Zhenan Gu, Lian-Mao Peng, J.-L Wu, and Zhonghui Xue. Investigation on the structure and electric properties of bucky onions. *Acta Physico - Chimica Sinica*, 17, 2001.
- [67] F. Rozpłoch, J. Patyk, and J. Stankowski. Graphenes Bonding Forces in Graphite. *Acta Physica Polonica A*, 112(3):557, 2007.
- [68] F Rozpłoch, J Patyk, and P Szroeder. New point of view on epr-line shift in carbon materials. *Molecular Physics Report*, 37:24–28, 2003.

Supplemental material: Simulation of multi-shell fullerenes using Machine-Learning Gaussian Approximation Potential

C. Ugwumadu,^{1,*} K. Nepal,¹ R. Thapa,¹ Y. G. Lee,¹ Y. Al Majali,² J. Trembly,² and D. A. Drabold^{1,†}

¹*Department of Physics and Astronomy,
Nanoscale and Quantum Phenomena Institute (NQPI),
Ohio University, Athens, Ohio 45701, USA*

²*Russ College of Engineering and Technology,
Ohio University, Athens, Ohio 45701, USA*

(Dated: December 15, 2022)

Sect. S1. Description of Animations produced for the buckyonion models

To aid in visualizing some of the discussions in the paper, we have produced some animations for some buckyonion models. The animations can also be found [here](#) or by visiting the url: https://people.ohio.edu/drabold/cepa_movies/.

1. BO300_mov.mp4 and BO1374_mov.mp4 files show the buckyonion formation process for BO₃₀₀ and BO₁₃₇₄ respectively. The outer, middle and inner shells are colored green, red, and blue in the BO1374_mov.mp4 file respectively. The green (red) colored atoms in the BO300_mov.mp4 file represent the outer (inner) shell.
2. BO_growthProcess.mp4 shows the clustering and growth process for 540 randomly distributed atoms within a 720-atom fullerene isomer. The shells are colored the same as described for the BO1374_mov.mp4 file. The pentagon rings in the 720-atom fullerene isomer are colored black to show their positions.
3. TotalChgDensity.mp4 and PiChgDensity.mp4 shows the progression of the charge density in the -xz plane for all bands and only the π -bands respectively. The mid-section discussed in the manuscript is at $y = 11.51 \text{ \AA}$

Sect. S2. Supporting Tables and Figures

TABLE S1: Ring-size analysis for the buckyonion models.

Models	Layers	Ring size:				
		5	6	7	8	9
BO ₆₀	s_1	12	20	0	0	0
BO ₃₀₀	s_1	15	22	3	0	0
	s_2	26	74	14	0	0
BO ₅₄₀	s_1	26	50	12	1	0
	s_2	62	85	28	8	2
BO ₈₄₀	s_1	6	1	0	2	1
	s_2	34	84	20	3	0
	s_3	68	148	40	11	0
BO ₁₃₇₄	s_1	27	34	14	3	1
	s_2	25	189	13	2	0
	s_3	50	292	36	3	0
BO ₂₁₆₀	s_1	15	20	10	2	1
	s_2	36	291	25	0	5
	s_3	55	380	32	2	5
BO ₃₇₇₄	s_1	31	91	17	4	4
	s_2	47	183	26	5	4
	s_3	112	333	80	18	6
	s_4	179	422	123	24	7

* cu884120@ohio.edu

† drabold@ohio.edu

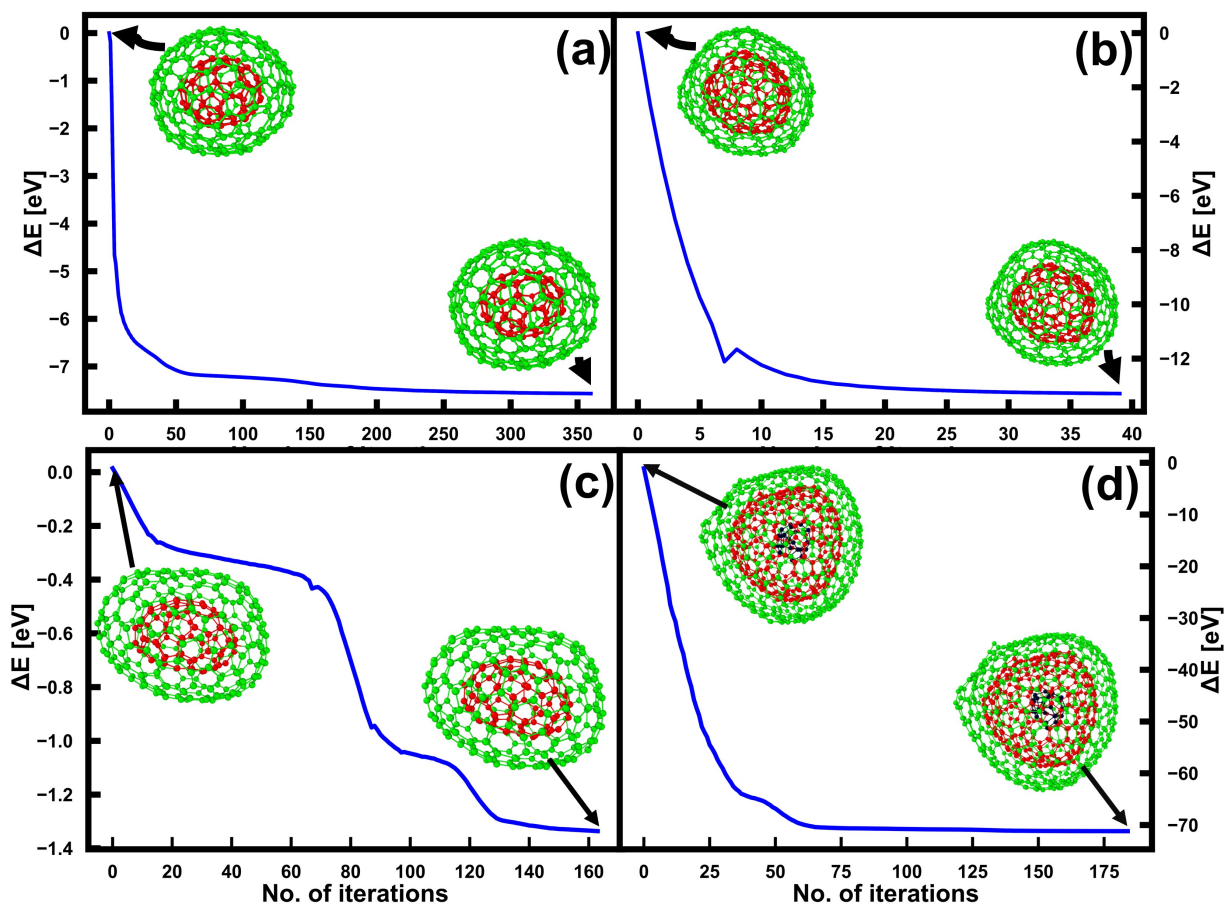


FIG. S1: Plots of the energy difference (ΔE) against the Conjugate gradient (CG) iterations carried out using VASP on BO₃₀₀ (a) and BO₅₄₀ (b). SIESTA was used for the BO₃₀₀ (c) and BO₈₄₀ (d) models as well. The insets in a-d represent the models before and after CG relaxation.

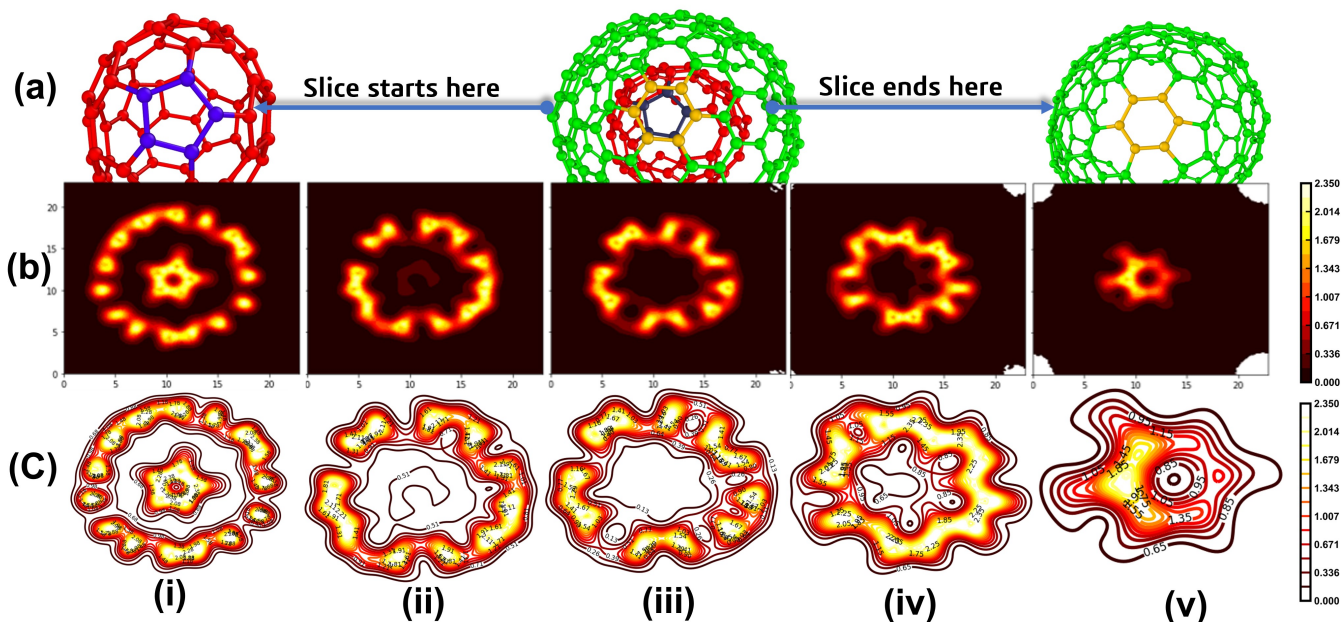


FIG. S4: The distribution of the charge density [in $e^-/\text{\AA}^3$] for other end of the BO_{300} model considered in Fig. 8 in the main manuscript. In the first row (a), the first column (a (i)) starts with a pentagon (yellow) in the outer shell (green), and the fifth column (a(v)) first slice in the inner shell (red) showing 2 carbon atom. The second and third rows (b and c) show the heat map (b (i - v)) and contour values (c (i - v)) of the charge density for 5 slices in columns i - v. The charge distribution in the opposite end of the plane considered here is discussed in the main manuscript.

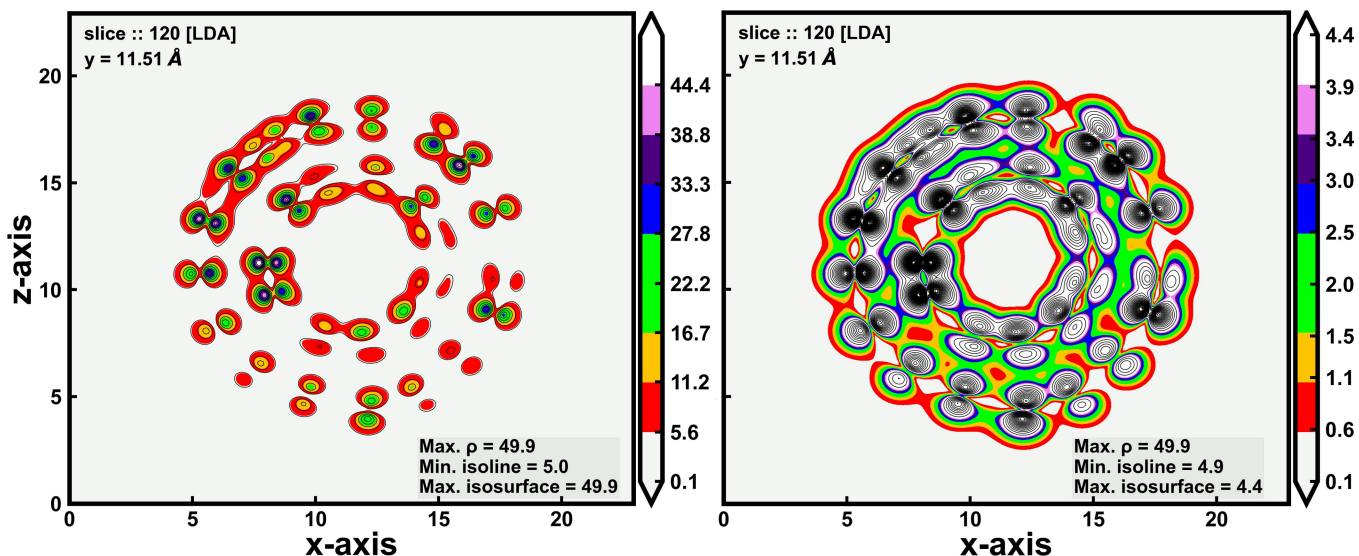


FIG. S5: The delocalized π -electrons in the mid-section of the $-xz$ plane in a BO_{300} model using LDA functional. The values of the charge density were scaled by a factor of 100. The left plot shows the entire range of π charge density values in that particular slice and the atoms are positioned in the center of the dumbbell shape which is formed with contour lines with a minimum threshold cutoff of $0.034 e^-/\text{\AA}^3$. The light-blue region in-between the shells (gallery) suggests that the value of the delocalized electron charge density is less than $0.074 e^-/\text{\AA}^3$. The left plot indicates that the value π electron charge density in the gallery ranges majorly between 0.012 to $0.023 e^-/\text{\AA}^3$ and has values up to $0.034 e^-/\text{\AA}^3$ when there are atoms that are positioned opposite each other in different shells.